The use of test structures to perform chip level characterisation studies of Ni and NiFe electrochemical deposition

The use of test structures to perform chip level characterisation studies of Ni and NiFe electrochemical deposition

J. Murray, R. Perry, J.G. Terry, *Senior Member, IEEE*, S. Smith, *Senior Member, IEEE*, A.R. Mount, A.J. Walton, *Senior Member, IEEE*

***Abstract*— This paper describes the first use of test structures designed to characterise the fundamental properties of nickel and nickel-iron alloy films deposited using electroplating. The structures are used to perform a chip-level investigation into the effects of electrolyte bath composition on the characteristics of deposited films. The advantage of this methodology is that each electrolyte change does not require the replacement of the large volume bath associated with wafer scale manufacturing investigations, thereby making the characterisation and optimisation of electroplating baths far less time consuming, and considerably more cost effective.**

Keywords—Electrodeposition; MEMS; Nickel; NiFe; Permalloy; optimisation; stress; strain; test structures;

I. Introduction

NiFe alloy films are widely used in microfabricated magnetic components to increase their inductance, and are typically applied using electrochemical deposition (ECD) due to its low coercively and high magnetisation saturation [1]. To help understand the electroplating of these alloys for components such as microinductors it is first necessary to characterise the parameters controlling both Ni and NiFe deposition. A standard electroplating bath such as a Semitool Raider has an electrolyte volume of 75 litres, which makes changing the plating bath an expensive and time consuming procedure as the whole system needs to be flushed. The ability to optimise the bath using the same test structures as those used to optimise wafer–scale plating is an attractive option. This paper describes the use of test structure chips specially designed to develop electroplating processes using 100 ml electrolyte volumes.

An important challenge is the fundamental understanding of the anomalous co-deposition of NiFe, as the less noble metal Fe, deposits preferentially to the more noble metal Ni [2]. This behaviour is abnormal, as nickel would plate at a faster rate in a typical aqueous solution when electroplated individually. As a result of this phenomenon a $Ni_{80}Fe_{20}$ plating bath is usually prepared with 40 times as much nickel as iron [2,3]. Many explanations have been proposed for this anomalous co-deposition of NiFe [4-8]. The additives and electrodeposition conditions also influence both the magnetic properties and the stress [9-11]. Most baths for this purpose use saccharin as an additive which results in a decrease in grain size and residual stress [11,12].

The ultimate reliability of a device lies in the optimum properties of a plated film. In the semiconductor and MEMS industry, accurate characterisation of residual stress in these films is therefore important to successfully predict the final device performance. High stress can induce delamination and the peeling of thin films and investigations into the control of stress when electroplating Permalloy layers have identified [13] that a low concentration plating solution ($NiCl_2$ 23.5 g/l and $FeCl_2$ 1 g/l) helps to lower the internal stress of the deposited layer, and the stress could be further decreased with an increase of additive (saccharin) content. All these stress measurements were made using the wafer curvature technique [14] which gives the overall value of stress in the wafer. The following section presents the background on previously employed stress measurement techniques and discusses their relative advantages and disadvantages.

II. Background

The wafer curvature technique [14], which is widely used in the silicon industry for measuring stress in thin films has some limitations. Firstly, depending on the measurement system the films may be required to be deposited on one side of the wafer whilst the other side, usually also polished for reflectivity, is scanned using a laser. Secondly, wafer bending decreases as the square of the wafer thicknesses, so the sensitivity to changes in stress in thin films decreases with larger wafers with greater thickness. Thirdly, this technique measures the sum of the stress induced by all films in the case where there are multiple layers. The thermal mismatch between all films will then have to be considered which adds to the complexity of analysing results. For each measurement the wafers have to be loaded in exactly the same position and this is also a potential source of error as wafers seldom have a perfect symmetry. A major issue is that this method reports the overall (averaged) stress of monolayer blanket films on substrates. Spatial variations in stress due to non-uniform process factors therefore cannot be investigated using wafer curvature.

Stress measurement devices/test structures were developed in tandem with surface micromachining techniques [15]. An early method used strain (deformation) of the material to quantify strain, e.g. double supported bridges [16]. However, these structures bend only if the compressive strain was above the critical Euler value [17] and so a large number of bridges of different lengths have to be fabricated for a satisfactory resolution of strain. The second type of direct strain measurement structures were the T and H-type structures fabricated by Allen et al [18]. These methods were prone to deflection extraction errors and as a result scaling them down for spatial variations measurements was never reported.

Lin and Goose [19,20,21] first devised mechanical devices that measured residual strain using an extension beam and a Vernier scale. These were designed so that when the structure is

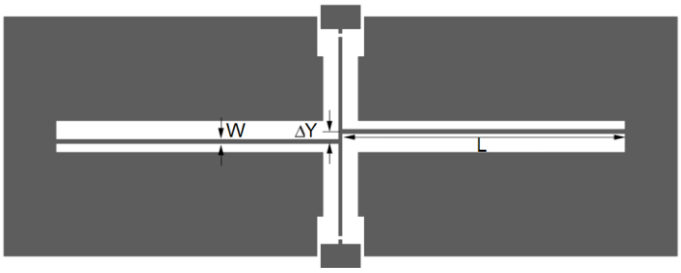

Fig. 1. A schematic layout of the strain test sensor showing the important dimensional parameters which control the sensitivity of the structure.

released by removing the underlying sacrificial layer, the residual stress in the film is released causing the indicator beam to defect. This enables the residual stress to be determined at different locations on a silicon wafer. A single structure, can therefore be used to determine both tensile and compressive stress using an optical microscope. This structure turns out to be very useful as the residual strain can be calculated without the knowledge of the underlying film properties.

Xin Zing et al. [22] introduced another variant of micro-rotating sensor with improved sensitivity though notches. In particular, when the magnitude of the residual stress was small, the micro-rotating structures could still make the measurement with a high accuracy of ±1 MPa [22,23]. Another approach [24] uses a load lever, a pair of torsion bars, supported by a 15×15mm frame and is based upon a two-step bulk micromachining process. Using equipment such as a nanoindenter or an AFM to displace the lever enables both strain and Young's modulus to be extracted.

The use of test structures has many advantages over the wafer curvature method. Localised measurements can be performed on a wafer or chip, using multiple structures, because of their small size. This can be employed to obtain useful spatial information related to any abnormalities in the deposition process. Strain test structures are also compatible with familiar CMOS technology, enabling measurements in real time during the wafer fabrication process cycle. Another major advantage is the relationship between the substrate thickness and stress can also be neglected, enabling small changes in stress and elasticity to be measured without of any consideration of the underlying layers, even if the film being evaluated is very thin (~1 μm).

This paper reports the use of rotating test structures electroplated on individual chips for characterisation. These have facilitated the evaluation of the plating process and a determination of factors such as deposition efficiency, resistivity and strain, all of which are important parameters for electroplated films. The key benefit of using test chips rather than full wafers for this initial process development is that it enables different electrolyte compositions to be rapidly evaluated in an efficient and cost effective manner, while at the same time making it feasible to more widely explore the parameter space.

III. TEST CHIP DESIGN AND FABRICATION

The test structure architecture used in this work is shown in Fig. 1 [25,26] and consists of two expansion arms and a pointer arm of width (W=8 μm) underneath which a sacrificial layer has been removed. Depending on whether the arms are in compression or tensile the pointer arm rotates in a different direction. From $Y = \sigma/\varepsilon$ the stress (σ) is proportional to strain (ε), which can be calculated from the angle of rotation (θ) using

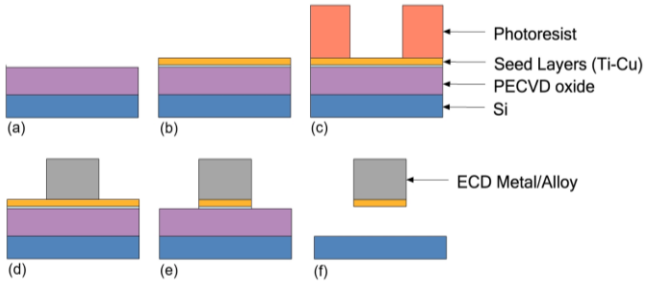

Fig. 2. Schematic process flow showing cross sections through a test structure at each stage of fabrication (a) PECVD oxide deposition (b) seed layer (c) resist patterning (d) electrodeposition and resist removal (using acetone), (e) seed layer wet etch using 1% HF, (f) test structure release using HF vapour etch.

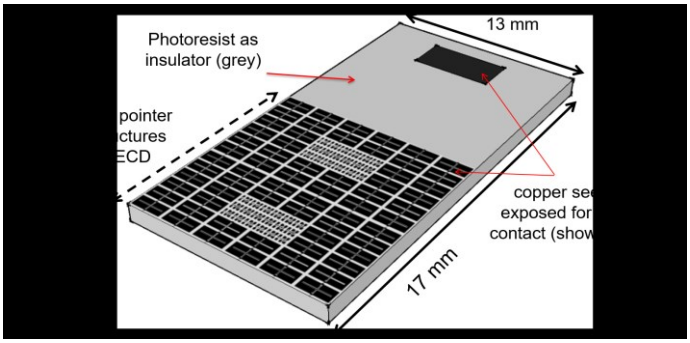

Fig. 3. Schematic drawing of a test structure die with 64 strain sensors and 36 electrical test structures giving a combined plating surface area of 0.765 cm^2. Ref [25] provides more details of the test chip layout.

($\varepsilon = \theta\ \Delta Y/L$) as described in [25], where, ΔY is the arm separation and L= 850 μm is the designed arm length without stress. The rotating strain structure has been selected for the straightforward simple surface micromachining process, its small footprint and the availability of an automated procedure for measuring the angle of rotation (Note: in this paper we have reported the angle of rotation – reference [27] reports the procedure to determine the stress). The design also provides locations for the local measurement of Young's modulus using a nanoindenter [27]. Clearly electroplating on a patterned chip more fully replicates the full wafer MEMS/semiconductor process than simple blanket depositions on a small substrate or flexible strips for stress evaluations [28].

The test chip design has been previously replicated across a 200 mm wafer using an 8 μm thick photoresist layer to form the mould for wafer-scale electroplating. This chip design successfully characterised the wafer-scale process confirming the value of the test structures and the chip layout for process development [25,27].

Fig. 2 shows cross sections through the strain structures at each stage of the process. The wafer was initially coated with a 700 nm thick layer of PECVD SiO_2 (Fig. 2(a)), followed by a sputtered Ti:Cu:Ti stack (Ti 30 nm, Cu 200 nm, Ti 30nm), which formed the seed layer for electroplating (Fig. 2(b)).

As the diced chips are to be individually plated, an additional region on chip must be exposed to accommodate the electrical contact to the potentiostat used to electroplate the chip (see Fig. 3). Therefore, two extra masks were printed on acetate, which were used to expose and develop a contact pad large enough to enable simple electrical connection using a crocodile clip. This provided the required electrical connection to the seed layer for electroplating. Following photoresist patterning (Fig. 2(c)) the

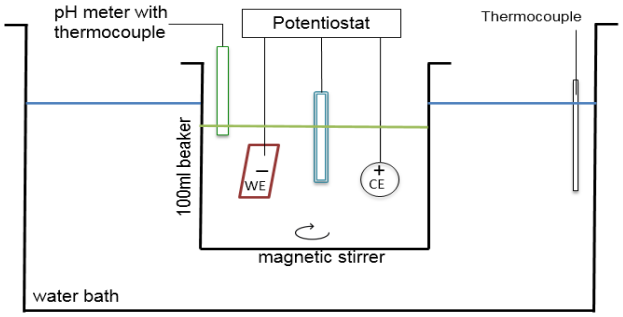

Fig. 4. Schematic drawing of the experimental setup for the ECD study.

chips were singulated (Fig. 3) using a dicing saw in readiness for evaluation of the electroplating process.

Before electroplating the chip, the exposed titanium layer was first removed to reveal the copper seed layer in preparation for ECD. A schematic drawing of the diced test structure die is presented in Fig. 3 showing the contact used for electroplating the test structures.

IV. Characterisation Setup

The configuration used for the single chip ECD of Ni/NiFe is detailed in Fig. 4. The electroplating and measurement system consisted of a computer controlled potentiostat/ galvanostat (Metrohm Autolab PGSTAT302), pH meter (Mettler Toledo – FE20), digital thermometer and a three electrode system with a saturated calomel electrode (SCE) as reference electrode (RE), a pure nickel counter electrode (CE – anode) and a test structure chip as the working electrode (WE – cathode). The galvanostat also recorded the precise potential, E, with respect to the SCE during the ECD process, and these data have also been analysed in the study.

Although only significant when carrying out prolonged ECD, a nickel CE was used instead of the standard inert platinum CE in order to be consistent with plating procedures used for wafer-scale processes. This setup was kept identical for all experiments with the spacing between the CE and WE set at 2.5 cm. The cell used was a 200 ml beaker containing 100 ml of electrolyte, temperature controlled by insertion in a water bath. The solution was sparged to remove dissolved air by bubbling argon gas through for about 20 minutes. For most tests, the current density applied ranged between 5 and 40 mA cm^{-2}, the temperature was set at 25 °C and the pH of the electrolyte was maintained at a value between 2.4 and 2.6. The pH tended to increase during ECD as a result of hydrogen evolution at the cathode surface and so this was monitored and kept constant by the addition of 1% v/v aqueous HCl solution.

The electrolyte bath combinations evaluated are detailed in Table 1. A fresh bath was used for each batch of dice and the plated samples were rinsed with deionised water and dried using a flow of nitrogen gas before further characterisation.

TABLE I
ELECTROPLATING BATH COMPOSITIONS

Bath	Bath Composition
1	$NiCl_2$
2	$NiCl_2$-boric acid
3	$NiCl_2$-$FeCl_2$
4	$NiCl_2$-$FeCl_2$-boric acid
5	$NiCl_2$-$FeCl_2$-boric acid-saccharin

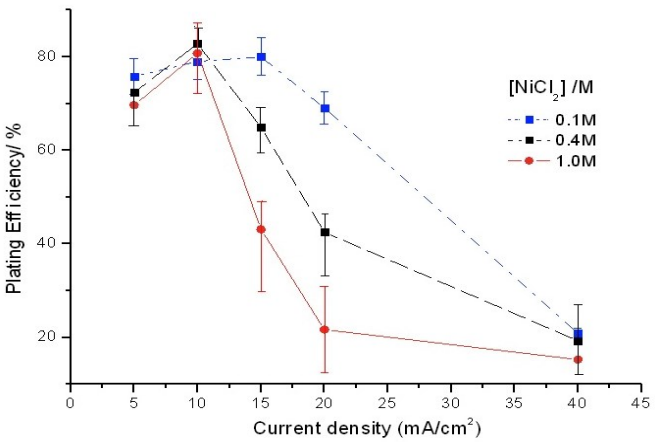

Fig. 5. Efficiency of nickel baths composed of different $NiCl_2$ compositions 0.1 M, 0.4 M and 1.0 M at pH of 2.6. The error bars represent the standard error.

The plating current efficiency was first established from the mass gain of the cathode (the test chip in Fig. 3) by simply comparing the weight of the chip measured before and after the ECD process. After this the photoresist was stripped (Fig. 2(d)) and the seed layers were etched (Fig. 2(e)) in preparation for the release of the strain test structures by HF vapour etching of the sacrificial SiO_2 layer (Fig. 2(f)) as detailed in reference [25].

The pointer arm rotation of the strain test structures was determined from an image of the structure captured using a microscope camera. This was analysed using an image analysis algorithm written in LabVIEW, which is described in references [27,29]. To ensure that changes in arm geometry did not affect the results, a single device geometry was analysed (separation ratio $\Delta Y/W = 1.75$).

V. Effects of Plating Conditions and Additives

A. Effect of pure nickel concentration on plating

A limited number of ECD tests were first performed at room temperature, to investigate the effect of changing nickel(II) chloride concentration on the plating efficiency and the resulting film strain. For simplicity, the bath setup was kept free of any additives or surfactants. Three sets of test structure chips were plated using $NiCl_2$ solutions of concentrations 0.1 M, 0.4 M and 1.0 M. Within each set, chips were plated at 5, 7, 10, 20, 40 mA.cm^{-2} current densities. This electroplating was carried out galvanostatically at the chosen current density, for the time calculated to achieve a target thickness of 5µm at 100% plating efficiency. These test chips enabled the ready extraction of overall plating efficiency, presented in Fig. 5 for the different baths compositions.

An interesting observation from Fig. 5 is that the efficiency can be seen to increase with plating current density until it falls sharply to <40% for all three nickel baths. A peak value of (85 ± 8%) between 10 and 20 mA.cm^{-2} is also observed. Overall, the efficiency is also seen to drop with increasing nickel concentration.

Fig. 6 shows plots of the observed potential as a function of time for the set of samples plated in 0.1 M nickel(II) chloride. The current was initially held at 0 mA.cm^{-2} to observe the open circuit potential (OCP). During these experiments the OCP prior to deposition was observed to be -0.24 V. A current is then set and the measured potential sharply decreases. During

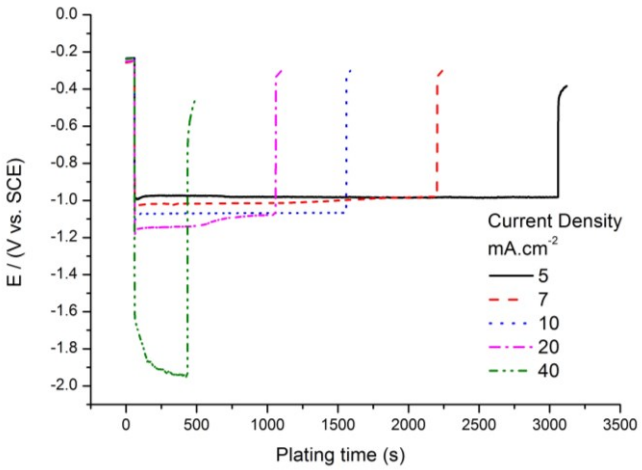

Fig. 6: Potential vs. time plots of samples plated using 0.1 M $NiCl_2$ (aq) for a range of current densities.

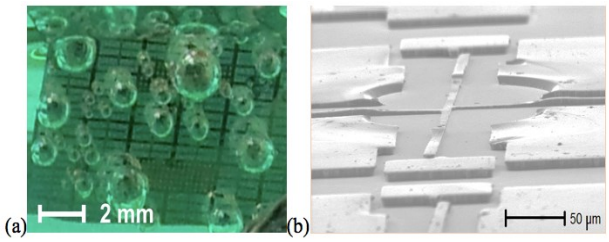

Fig. 7. (a) Camera image of a test structure chip being plated (at 10mA.cm^{-2}) showing hydrogen bubbles evolving during deposition (b) SEM image of the region of the test structure (after stripping photoresist) where a hydrogen bubble was seen to be trapped.

deposition both hydrogen and nickel are produced, the ratio of which is determined by the applied current. As the deposition of nickel is kinetically unfavorable the proportion of nickel deposited decreases as the current density increases (Fig. 5). In the early stages (<5 s) of deposition the underlying metal for deposition is the copper seed layer and as time progresses the electrode surface becomes covered in a nickel layer. This is observed as a change in potential at the start of plating and is more prolonged at lower current densities, which is expected during the longer transition from Ni on Cu (seed layer) to Ni on Ni deposition. A steady state potential is then reached when depositing Ni on Ni. After when the applied current is returned to 0 mA the potential does not immediately returns to a constant value, this is likely due to the time required for hydrogen to diffuse away from the electrode and the surface pH to return to the bulk value.

The plating potentials were also observed to become progressively more negative with increasing current density (5, 7, 10 and 20 mA.cm^{-2}). However, at 40 mAcm^{-2} a major potential decrease is recorded, which is significantly different from these other samples. This potential drop can be regarded as the domination of the hydrogen evolution reaction (equation 1) at high currents over nickel deposition, which has also been reported by Song et al. [30]. With significant hydrogen evolution the pH will rise to an extent where $Ni(OH)_2$ can be precipitated (equation 2) [31].

$$H_2O + e^- \rightarrow 1/2\ H_2 + OH^- \quad (1)$$

$$Ni^{2+} + 2OH^- \rightarrow Ni(OH)_2 \quad (2)$$

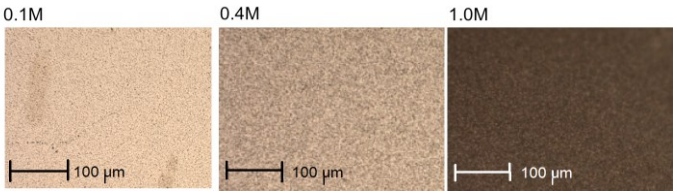

Fig. 8. Magnified microscope images (×100) showing the texture of samples plated at 10 mA.cm^{-2} from pure $NiCl_2$ solutions with concentration 0.1 M, 0.4 M and 1.0 M respectively.

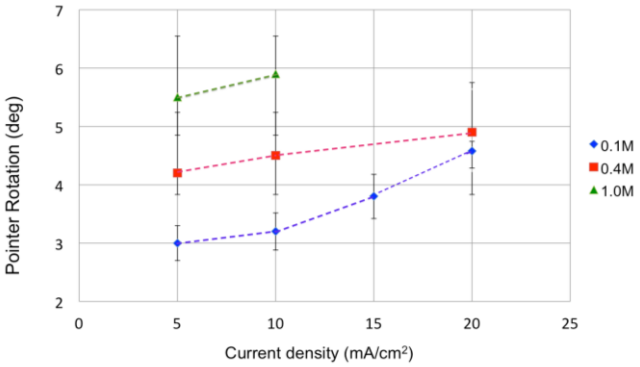

Fig. 9. Pointer rotations of nickel test structures plated in different $NiCl_2$ compositions 0.1 M, 0.4 M and 1.0 M at different current densities and a pH of 2.6.

Consistent with the observed plating efficiencies, it is interesting that hydrogen bubbles, were observed on all plated samples.

A typical image of a chip being plated is shown in Fig. 7(a) where bubbles were observed which adhered to the surface and gradually increased in diameter during plating. As expected, at 40 mA.cm^{-2}, bubbles were seen to evolve most vigorously and rapidly from the surface.

An SEM image of a structure plated in the 0.4 M $NiCl_2$ bath at 10 mA.cm^{-2} is shown in Fig. 7(b). This image shows the effects on part of a test structure, where a hydrogen bubble has been trapped. A clear circular depression is visible where little or no nickel has been deposited. This suggests that the presence of a static hydrogen bubble on the surface which physically inhibits nickel deposition. This may further lower the overall plating efficiency of the bath as the effective current density is increased.

Magnified images focusing on the film texture are shown in Fig. 8, which identify that the texture changes with increasing concentration of $NiCl_2$. The inclusion of an insoluble nickel compounds (e.g. $Ni(OH)_2$) in the film and the trapped electrolyte (seen as a greenish white finish) may have also contributed to the variation in grain morphology and film appearance. The different OCP after deposition may also indicate the increased presence of these species. Further analysis is required to fully confirm these findings.

The primary advantage of using the test chips is to rapidly evaluate the strain against these variables. The test structures were released by etching the underlying seed layer and the rotation of the pointer arms determined optically [27]. The pointer rotation was measured as a function of the plating current density for three concentrations of $NiCl_2$ and the results presented in Fig. 9.

A clockwise rotation, indicating tensile stress, was observed for all samples. The highest mean rotation (6.0°) was measured

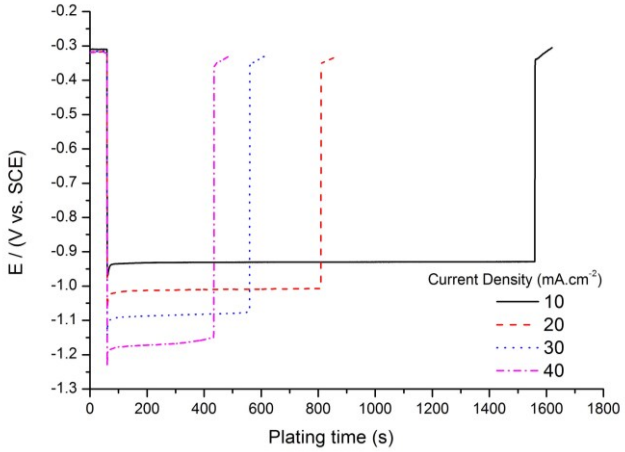

Fig. 10. Typical potential - time plots showing the effect of current density on Nickel plating from a bath containing $NiCl_2$ (0.4 M) and boric acid (0.4 M).

for the 1.0 M $NiCl_2$ bath at 10 mA.cm^{-2}, while the lowest (2.6°) was obtained for 5 mA.cm^{-2} plated in a 0.1 M $NiCl_2$ solution. On average, mean rotations increased both with $NiCl_2$ concentration and with plating current density, which clearly indicates that plating parameters directly influence the development of the intrinsic stress.

From the results presented, it can be concluded that both relatively low strain films and high efficiency plating can be obtained from a pure nickel bath with concentrations between 0.1 M and 0.4 M, plated at current densities ranging between 5 and 20 mA.cm^{-2}. As hydrogen evolution has also been shown to be a factor which influences the plating efficiency, it is not unreasonable to speculate that the resulting changes in surface reaction may also affect the resulting structural properties of nickel.

B. Effect of boric acid in pure nickel solution

Boric acid has been used in nickel/nickel-iron plating for decades and many researchers have studied its effect. However, its influence on nickel deposition is complicated and remains unclear. The suggested effects for boric acid can be broadly categorised into four areas; (a) action as a buffering agent [32], (b) action as a catalyst [33], (c) suppression of the hydrogen evolution reaction (HER) [28,34], and (d) reduction of passive film formation [34,35,36].

The aim in this work was to examine the role of boric acid in the suppression of the HER through a systematic study of the effect of boric acid on the plating efficiency and relate this to film strain. The first batch of samples were plated with nickel using a bath containing 0.4 M $NiCl_2$ and 0.4 M boric acid, at different current densities (10, 20, 30 and 40 mA.cm^{-2}). A second batch was plated at 20 mA.cm^{-2} but with varying boric acid concentrations (0 to 0.8 M). The target film thickness for all samples was again 5µm. Fig. 10 presents the potential vs. time plots obtained for the first batch of samples, which shows that a steady plating potential was achieved for the three current densities except at 40 mA.cm^{-2}, where there was slight variation. Apart from the transient voltages recorded on connection, the highest negative (cathodic) potential was recorded for this sample, of -1.17 V during the middle of the plating process. The initial OCP was consistent for all plating samples (at -0.32 V) and comparable with experiments for $NiCl_2$ alone. The OCP after deposition again was observed to become more positive after deposition was ceased.

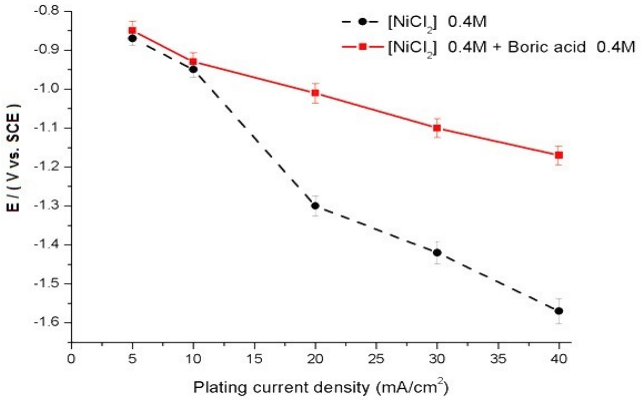

Fig. 11. A comparison of the steady-state plating potential vs. plating current density of baths containing only $NiCl_2$ (0.4 M) and $NiCl_2$ (0.4 M) + boric acid (0.4 M).

However, the trends and values of the OCP after plating were much more consistent than the observations in pure $NiCl_2$, which were presented in Fig. 6. During plating there were far fewer hydrogen bubbles seen evolving in the nickel/boric bath producing a denser and more uniform Ni film. A consistent OCP across all current densities applied suggests boric acid prevents the formation of the more passive nickel hydroxide species preventing them from influencing the OCP. Without boric acid, the films were blemished due to excessive hydrogen evolution and associated hydroxide formation both of which may incorporate within the film and make the final OCP vary from sample to sample. The presence of boric acid clearly enabled relatively efficient Ni plating at higher current densities, which could not be achieved in its absence.

These observations can be further enhanced through the comparison of the steady-state cathodic potential (E) for pure Ni and Ni-boric baths for different plating current densities (Fig. 11). It can be observed that the potentials for low current densities (5 and 10 mA.cm^{-2}) are similar, while at plating current densities higher than 10 mA.cm^{-2}, a large potential drop (~0.3 V) is observed for the pure $NiCl_2$ bath attributable to hydrogen evolution. In the presence of boric acid, no such potential drop exists, which suggests the suppression of hydrogen formation and the retention of relatively efficient Ni plating.

The effect of boric acid concentration on the plating potential is shown in Fig. 12. The OCP of –0.33 V and a plating potential of –1.03 V showed no significant change between different concentrations of boric acid above 0.2 M, while the cathodic potential in the absence of boric acid was between 0.3 V and 0.4 V more negative. This demonstrates that at elevated current densities, boric acid inhibits hydrogen reduction. The fact that no change in the OCP is observed, with and without boric acid, also suggests there is no nickel-boric complex present in the bath.

Optical images of the sample plated at different current densities are shown in Fig. 13. It can be observed that films have a shinier finish when plating at 10 mA.cm^{-2}, while higher current densities display a slightly darker finish.

Pointer rotations and plating efficiencies were extracted from these optical images of the test structures and each plotted as a

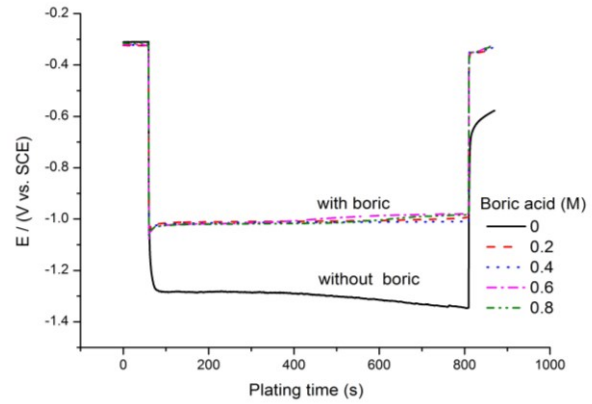

Fig. 12. Potential-time plots for Ni ECD of samples plated in different boric acid concentrations ($NiCl_2$ (0.4 M).

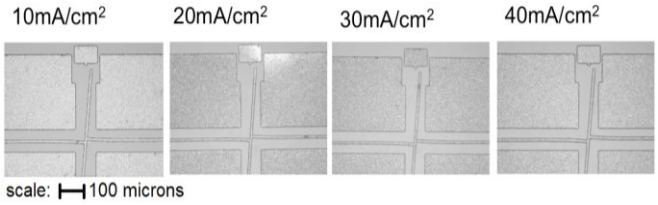

Fig. 13. Microscope images of Ni test structures plated at different current densities.

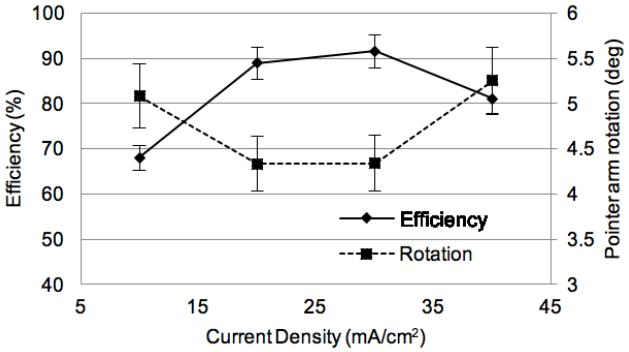

Fig. 14. Plated efficiency and pointer rotations with current density for a solution containing 0.4 M $NiCl_2$ and 0.4 M Boric acid.

function of current density (Fig. 14). A maximum efficiency plateau of 92 ± 3 % for 20-30 mA.cm^{-2} is observed, followed by a slight decline to 81 ± 4% at 40 mA.cm^{-2}. The results suggest that the deposition of nickel is not mass transport limited for current densities below 30 mA.cm^{-2}.

Fig. 15 shows comparable data in the presence and absence of boric acid at 20 mA cm^{-2}. It can be observed the plating efficiency was lower without boric acid at 57 ± 6 % but increased with added boric acid until 0.4 M, where the efficiency appears to plateau at ~ 90%.

It is interesting that for these data there is a consistent decrease in the observed strain (pointer rotation, indicative of film stress) with increased plating efficiency. This suggests that hydrogen evolving during nickel deposition may be absorbed within the plated film creating defects, causing changes to the film morphology which may give rise to this stress. Armyanov [37] has previously claimed that the desorption of hydrogen co-deposited in the nickel film from a Watts bath was responsible for high tensile stress in the film.

The inverse correlation between these two quantities is confirmed in Fig. 16, which compiles all the data from these experiments. With the aid of the strain test structures, these data also confirm that strain and plating efficiency are correlated

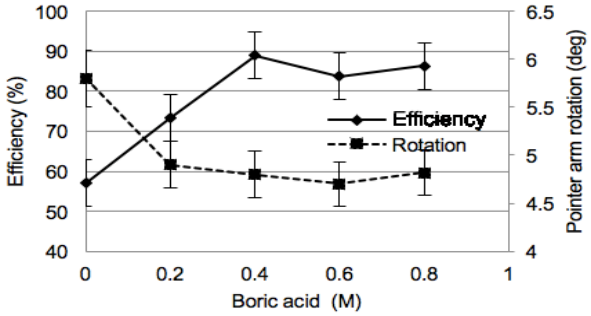

Fig. 15. Plating efficiency and pointer rotation with different boric acid concentrations for a solution containing 0.4 M $NiCl_2$ and a plating current density of 20 mA.cm^{-2}.

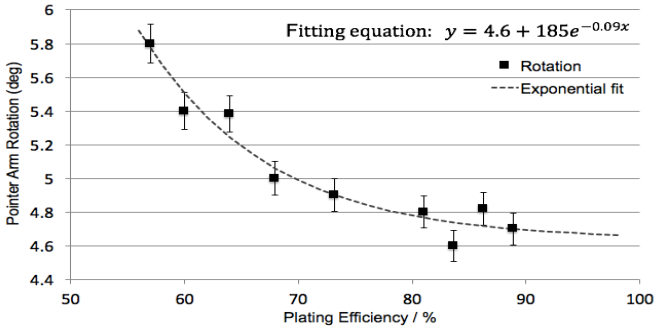

Fig. 16. Plot of pointer rotations against plating efficiency for a nickel bath at all boric acid concentrations; the exponential best fit was obtained through least squares analysis with $R^2 = 0.97$.

and that the eradication of hydrogen evolution/absorption is necessary to produce low stress Ni films as well as to increase plating efficiency.

C. Effect of boric acid in nickel-iron ECD

This section examines the effect of boric acid on the anomalous co-deposition of NiFe deposits and compares these results from those from the nickel only bath. To achieve a nickel-iron alloy (preferred target Permalloy $Ni_{80}Fe_{20}$), 3 g/l iron(II) chloride tetrahydrate was added to the original nickel solution and the effect on plating with and without boric acid investigated. The first sample was therefore plated using 0.4 M $NiCl_2$, 0.015 M $FeCl_2$ and no boric acid.

As soon as the plating commenced, it was observed that the cathode die became covered in a black deposit. This was accompanied by excess hydrogen evolution and the flaking of a powdery deposit. The efficiency of this plated sample could not be obtained as most of the loosely deposited material was removed during the deionised water rinse after plating. Similar effects were observed with the addition of boric acid up to 0.8 M. All the samples were carefully rinsed and weighed to reveal efficiencies of less than 30%. These initial observations suggest that the inclusion of iron has altered the deposition mechanism to such an extent that even the addition of boric acid (as a hydrogen suppressor) no longer has the same effect.

A comparison of plating potentials of pure Ni and NiFe alloy with and without boric acid has been compiled and is shown in Fig. 17. Firstly, a clear distinction between the initial OCPs can be observed which can be related to the inclusion of iron in the

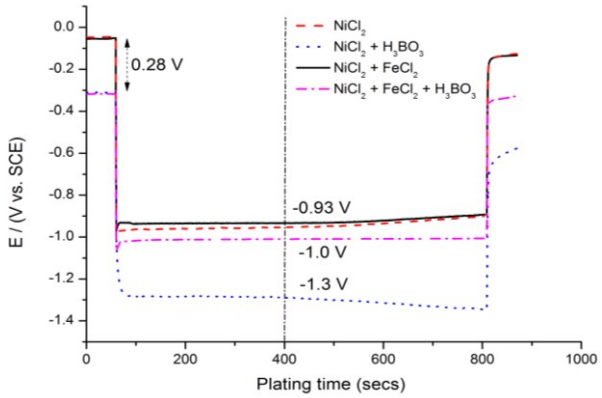

Fig. 17. Galvanostatic plots obtained from NiFe plating of die samples at 20mA.cm^{-2} in different bath chemistries.

bath. A similar change of 0.30 V OCP vs. SCE on a Pt rotating disc electrode has been reported in the literature as the existence of the Fe^{2+} / Fe^{3+} redox couple [38]. Secondly, the lack of a significant change between OCP before and after the addition of boric acid suggests no significant presence of either Ni-boric or Fe-boric complexes. Comparing the steady state plating potentials at the 400 second mark, a few conclusions can be drawn. Hydrogen evolution occurs in a pure nickel bath, and the potential rises up to –1.3 V. The addition of boric acid however, inhibits the production of hydrogen and encourages nickel reduction, which lowers the plating potential to –1 V. The presence of iron lowers the plating potential further to –0.93 V. This suggests the overall reduction reaction favours iron more than nickel (anomalous co-deposition of NiFe). Finally, adding boric acid to this bath makes no significant difference to the observed plating potential.

Pointer rotations arms were observed to have rotated clockwise to their maximum limit (9º) for all plated NiFe samples, both with and without boric acid. The inclusion of iron has, therefore, drastically changed the plating surface chemistry and increased the intrinsic strain of the films by more than 130%.

In nickel baths, the addition of boric acid (up to 0.4 M) was observed to improve the plating efficiency, but this could not be achieved in the presence of iron. All NiFe films showed signs of delamination, which is consistent with the very high tensile stress levels indicated by the pointer arm rotations. However, during deposition, it was observed that fewer bubbles were generated with the addition of boric acid, which suggests that boric acid was suppressing hydrogen evolution but the presence of iron hindered nickel reduction and resulted in films with high stress, susceptible to delamination and to an effective lower deposition efficiency. This observation also backs up previous studies reported in the literature [11,39], where the addition of boric acid in Permalloy plating solutions was not found to eliminate anomalous co-deposition, but rather induced more stress in the plated NiFe film, which also suggests its inclusion in the film during deposition can cause deformities.

D. Effect of Saccharin in nickel/iron/boric baths

One approach known to reduce the stress in electroplated films is the addition of saccharin to the electrolyte [11,12]. Hence the effect of saccharin on the strain in the film has also been investigated. Different concentrations of saccharin were added to the bath containing $NiCl_2$, $FeCl_2$ and boric acid; Table II summarises the bath compositions employed.

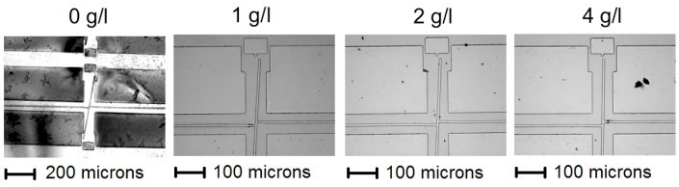

Fig. 18: Microscope images of NiFe samples plated in the bath containing $NiCl_2$, $FeCl_2$, H_3BO_3 (Table II) with the varying saccharin concentrations indicated above each image.

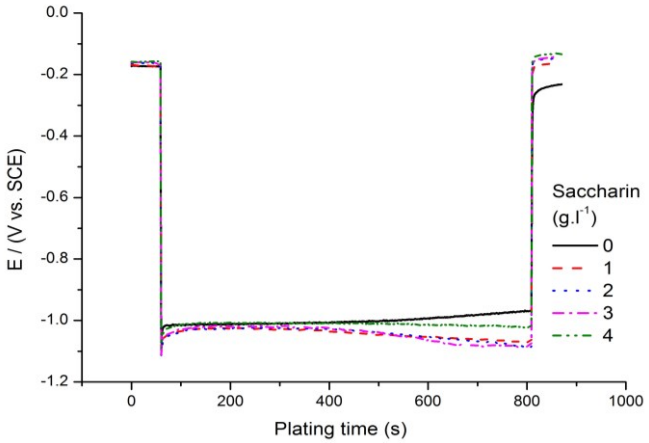

Fig. 19: Galvanostatic plot of nickel/iron alloy plating at 20 mA.cm^{-2} with the bath from Table II except for the stated saccharin concentrations.

TABLE II
NIFE-BORIC ACID-SACCHARIN BATH COMPOSITION AND CONDITIONS

Bath Contents	Parameters
$NiCl_2$ .6H_2O	0.4 M (95.2 g/l)
$FeCl_2$ .4H_2O	0.015 M (3 g/l)
Boric Acid	0.4 M (24 g/l)
Na-Saccharin	0-0.02 M (0-4 g/l)
Current Density (mA.cm^{-2})	20
Target thickness (μm)	5
Temperature (°C)	24 ± 1
pH (adjusted with 1% HCl)	2.6-2.8

Five bath samples were prepared with increasing saccharin concentrations. During deposition of each sample, fewer hydrogen bubbles evolved and there was no flaking or delamination. The deposited films also had a bright shiny finish as shown in Fig. 18.

Fig. 19 indicates that the initial OCPs for all five samples were roughly –0.16 V. During deposition, it was interesting to note an initial steady potential of –1.02 V for all samples, lasting 340 s, which then drifted to slightly differing potentials (more negative for saccharin) until the end. It was also interesting that there were differences in the OCPs observed after plating, consistent with differences of energies of the plated film surfaces.

These chips were then further processed to release the test structures and the strain rotation plots are presented in Fig. 20. The plating efficiency increased from 17 % (without saccharin) to around 90 % with the addition of 3 g/l of saccharin. Pointer rotations (strain) also significantly decreased with the addition of saccharin. The increase in saccharin concentration above a

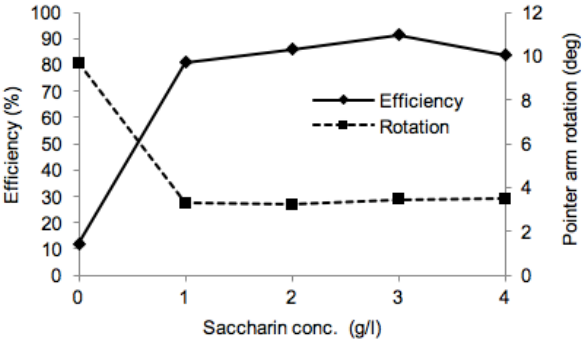

Fig. 20: Effect of saccharin on plating efficiency and strain of NiFe films; the baths were the same as those used in Fig. 19.

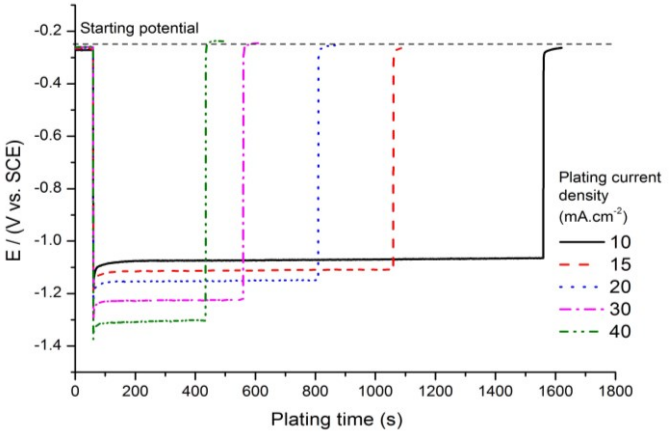

Fig. 21: Potential vs. time plots of NiFe plating at different current densities (10 - 40 mA.cm^{-2}); Bath as in Fig. 19 with saccharin (1 g.l^{-1}).

threshold of 1 g/l did not appear to cause a noticeable change in either the appearance or strain of the film.

The effect of plating currents was also investigated using the bath containing 1 g/l saccharin and the OCP is shown in Fig. 21. The first observation of this experiment is that little or no hydrogen gas bubbles were seen to evolve from the surface and the plating potentials were steady throughout the deposition. The samples also had a bright and shiny finish with no film delamination at any plating current density.

Fig. 22 shows the plating efficiency increases to a maximum of 90 % at 20 mA.cm^{-2} which then decreases for higher plating current densities. In this case the pointer rotation decreased with decreasing efficiency, which confirms that the origin of the strain in these NiFe films is unlikely to be a result of hydrogen evolution.

To investigate further, the iron composition in the films was measured and this was found to correlate with the strain as shown in Fig. 23. The correlation between the strain and percentage Fe was calculated as 0.98, which indicate a strong relationship between the two parameters. It is interesting that the Fe % in the film was also observed to change essentially linearly with the plating current density. A 32 % Fe proportion was achieved at 10 mA.cm^{-2} with 22 % Fe at 40 mA.cm^{-2}, which yields an approximately 3.3 % decrease in iron with every 10 mA.cm^{-2} increase in current density for a bath containing 0.4 M $NiCl_2$ and 15 mM $FeCl_2$.

From this study, saccharin concentration had only a minimal effect on plating efficiency and strain of NiFe films providing at least 1% saccharin was present. The lowest stress was achieved for a 40 mA.cm^{-2} plating current density while the highest

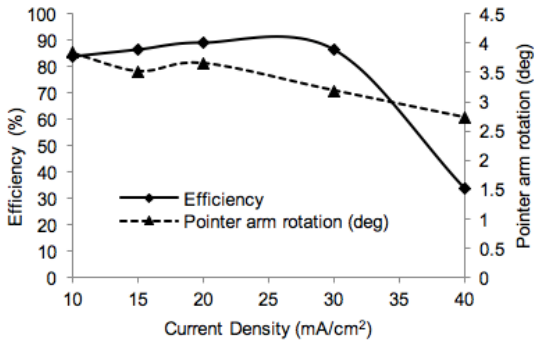

Fig. 22. The variation of plating efficiency and strain (pointer arm rotation) with plating current density for NiFe ECD. Bath as in Fig. 19 with saccharin (1 g/l).

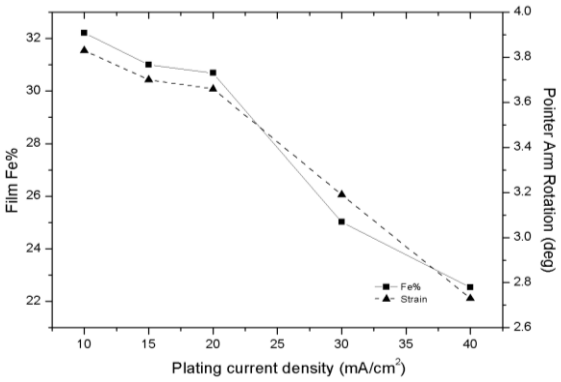

Fig. 23. The effect of plating current density on the film Fe% and strain (Bath chemistry as presented in TABLE II with 1 g/l saccharin).

efficiency (>90%) was obtained for a plating current density of 20 mA.cm^{-2}.

VI. Conclusions

This paper describes the first use of a test chip designed specifically with structures for the rapid evaluation of the fundamental properties of films deposited using electroplating. The 1.3 × 1.7 cm Si chips includes test structures, which have enabled the strain in Ni and NiFe films to be characterised within a 100ml of electroplating solution in a beaker level setup. This has enabled an efficient investigation of numerous bath chemistries, which has demonstrated how small changes in the plating conditions can lead to changes in film characteristics such as the intrinsic stress, texture and composition. One added advantage of this approach is that the same chip design can be used when scaling up the process to full wafer processing.

The effect of hydrogen evolution has been shown to be a prominent factor influencing the plating efficiency and also the resulting structural properties of nickel plated using a pure nickel bath. Low stress nickel films were achieved using a low concentration of $NiCl_2$ (0.1 M to 0.4 M) plated at low current densities (5 - 20 mA.cm^{-2}). For nickel films it was shown that the degree of strain strongly correlated with plating efficiency (and hence the extent of the HER).

The effect of boric acid and saccharin on NiFe has also been investigated. The work has identified the effect of current density as an important parameter in the control of the NiFe ratio and its correlation with film stress. Interestingly, the extent of hydrogen evolution was shown not to be a significant factor in the degree of strain for NiFe ECD. Table III summarises the optimum bath parameters and conditions to achieve low stress NiFe films.

This work has presented a platform for further optimisation and identified the process window available for Ni and NiFe electroplating in microelectronic and MEMS-related applications. It has demonstrated that the use of chip based test structures enables a rapid and cost effective approach, which effectively mimics the performance of industrial scale baths (70 litres) on a beaker scale. This work will facilitate the development of high efficiency electroplating of low stress NiFe films with numerous applications including MEMS microinductors and micro-switches.

TABLE III
OPTIMUM NIFE BATH PARAMETERS FOR LOW STRESS FILMS WITH FE (30-40%)

Bath Contents	Parameters
$NiCl_2 .6H_2O$	95.2 g/l
$FeCl_2 .4H_2O$	3 g/l (depends on target Fe %)
Boric Acid	24 g/l
Na-Saccharin	3-4 g/l
Current Density ($mA.cm^{-2}$)	20-30
Expected Fe%	20-25
Temperature (°C)	24 ± 1
pH (adjusted with 1% HCl)	2.6-2.8

ACKNOWLEDGEMENTS

We would like to acknowledge the financial support of the Edinburgh Research Partnership in Engineering, EPSRC/IeMRC Smart Microsystems (FS/01/02/10), a Spirit Studentship and Texas Instruments. Data presented in this paper can be accessed at http://dx.doi.org/10.7488/ds/2091.

REFERENCES

[1] P.C. Andricacos, L.T. Romankiw, H. Gerischer, C.W. Tobias, "Advances in electrochemical science and engineering", vol. 3, New York, p 227, 1994.

[2] D. Gangasingh, J.B Talbot, "Anomalous electrodeposition of nickel-iron", Journal of the Electrochemical Society, Vol 138, No 12, pp 3605–3611, 1991.

[3] J. Horkans, "On the role of buffers and anions in NiFe electrodeposition", Journal of the Electrochemical Society, vol 126, No 11, pp 1861–1867, 1979.

[4] M.J. Nicol and H.I. Philip, "Underpotential deposition and its relation to the anomalous deposition of metals in alloys", Journal of Electroanalytical Chemistry and Interfacial Electrochemistry, Vol 70, No 2, pp 233–237, 1976.

[5] M. Matlosz, "Competitive adsorption effects in the electrodeposition of iron-nickel alloys", Journal of the Electrochemical Society, Vol 14, No 8, pp 2272–2279, 1993.

[6] A. Brenner, "Electrodeposition of alloys: principles and practices", Academic Press, 1963.

[7] W.C. Grande and J.B. Talbot, "Electrodeposition of thin films of nickel-iron ii. modelling", Journal of the Electrochemical Society, Vol 140, No 3, pp 675–681, 1993.

[8] R. Bertazzoli, D. Pletcher, "Studies of the mechanism for the electrodeposition of FeCo alloys. Electrochimica acta", Vol 38, No 5, pp 671–676, 1993.

[9] I.W. Wolf. Composition and thickness effects on magnetic properties of electrodeposited nickel-iron thin films. Journal of the Electrochemical Society, Vol 108, No 10, pp 959–964, 1961.

[10] Y. Sverdlov, Y. Rosenberg, Y.I. Rozenberg, R. Zmood, R. Erlich, S. Natan, Y. Shacham-Diamand, "The electrodeposition of cobalt–nickel–iron high aspect ratio thick film structures for magnetic MEMS applications", Microelectronic Engineering, Vol 76, No 1–4, pp 258 – 265, 2004.

[11] F.E.Rasmussen, J.T. Ravnkilde, P.T. Tang, O. Hansen, S. Bouwstra, "Electroplating and characterization of cobalt–nickel–iron and nickel–iron for magnetic microsystems applications", Sensors and Actuators A: Physical, Vol 92, No 1, pp 242–248, 2001.

[12] S-H Kim, H-J Sohn, Y-C Joo, Y-W Kim, T-H Yim, H-Y Lee, T Kang, "Effect of saccharin addition on the microstructure of electrodeposited Fe36 wt Ni alloy. Surface and Coatings Technology", Vol 199, No 1, pp 43–48, 2005.

[13] Y.H. Zhang,G.F. Ding, Y.L. Cai, H. Wang, B. Cai, "Electroplating of low stress Permalloy for MEMS. Materials Characterization", Vol 57, No 2, pp 121 – 126, 2006.

[14] P.A. Flinn, "Principles and applications of wafer curvature techniques for stress measurements in thin films", MRS Proceedings, Vol 130. Cambridge Univ Press, pp 41-55, 1988.

[15] M.A. Schmidt, R.T. Howe, S.D. Senturia, J.H. Haritonidis, "Design and calibration of a microfabricated floating-element shear-stress sensor", Electron Devices, IEEE Transactions on, Vol 35, No 6, pp 750–757, 1988.

[16] H. Guckel, D.W. Burns, C.C.G. Visser, H.A.C. Tilmans, D. Deroo, "Fine-grained polysilicon films with built-in tensile strain", Electron Devices, IEEE Transactions on, Vol 35, No 6, pp 800 –801, Jun 1988.

[17] W. Fang and J.A. Wickert, "Post buckling of micromachined beams. Journal of Micromechanics and Microengineering", Vol 4, No 3, pp 116, 1994.

[18] M.G. Allen, M. Mehregany, R.T. Howe, S.D. Senturia, "Microfabricated structures for the in situ measurement of residual stress", Young's modulus, and ultimate strain of thin films", Applied Physics Letters, Vol 51, No 4, pp 241–243, 1987.

[19] L Lin, "Selective encapsulations of MEMS: Microchannels, needles, resonators, and electromechanical filters", Master's thesis, Thesis, Department of Mechanical Engineering, University of California, Berkeley, 1993.

[20] L. Lin, A.P. Pisano, and R.T. Howe, "A micro strain gauge with mechanical amplifier", Microelectromechanical Systems, Journal of, Vol 6, No 4, pp 313–321, Dec 1997.

[21] J.F.L. Goosen, BP van Drieenhuizen, P.J. French, R.F.Wolffenbuttel, "Stress measurement structures for micromachined sensors", Tech. Dig. 7th Int. Conf. on Solid State Sensors and Actuators, Transducers 93, Japan, pp 7-10, 1993.

[22] X. Zhang, T-Y. Zhang, Y. Zohar. Measurements of residual stresses in thin films using micro-rotating-structures. Thin Solid Films, Vol 335, No 1–2, pp 97 – 105, 1998.

[23] X. Li, Guifu. Ding, T. Ando, M. Shikida and K. Sato, "Micromechanical characterization of electroplated permalloy films for MEMS", Microsyst Technol., Vol 14, pp 131–134, 2007.

[24] ASTM B975-Standard Test Method for Measurement of Internal Stress of Metallic Coatings by Split Strip Evaluation (Deposit Stress Analyzer Method), 2016, https://www.astm.org/Standards/B975.htm.

[25] S. Smith, N.L. Brockie, J. Murray, C.J. Wilson, A.B. Horsfall, J.G. Terry, J.T.M. Stevenson, A.R. Mount, A.J. Walton, "Analysis of the Performance of a Micromechanical Test Structure to Measure Stress in Thick Electroplated Metal Films", IEEE International Conference on Microelectronic Test Structures, 22-25 March 2010, Hiroshima, Japan, pp 80-85.

[26] G. Schiavone, J. Murray, S. Smith S, M.P.Y.Desmulliez,, A.R. Mount, A.J Walton, "A wafer mapping technique for residual stress in surface micromachined films", Journal of Micromechanics & Microengineering., Vol 26, No 9, pp 095013, 2016

[27] S. Lokhandwala, J. Murray, S. Smith, A.R. Mount, J.G. Terry, A.J. Walton, "Development of an Advanced System for Automated 200 mm Wafer Mapping of Stress Using Test Structures", ICMTS, Grenoble, 2017 pp. 125-130.

[28] Y. Tsuru, M. Nomura, and F. R. Foulkes, "Effects of boric acid on hydrogen evolution and internal stress in films deposited from a nickel sulfamate bath", Journal of Applied Electrochemistry 32, no. 6, 629-634, 2002.

[29] S. Smith, N.L. Brockie, J. Murray, G. Schiavone, C.J. Wilson, A.B. Horsfall, J.G. Terry, J.T.M. Stevenson, A.R. Mount, A.J. Walton, "Fabrication and Measurement of Test Structures to Monitor Stress in SU-8 Films," IEEE Trans. Semicon. Manuf., vol. 25, no. 3, pp. 346-354, Aug. 2012, doi: 10.1109/TSM.2012.2202797.

[30] Ki-Deok Song, Kwang Bum Kim, Seong Ho Han, and Hong Ke Lee. "A study on effect of hydrogen reduction reaction on the initial stage of Ni electrodeposition using EQCM", Electrochemistry Communications, Vol. 5, no. 6, pp 460–466, 2003.

[31] S.R. Jayashree, and P. Vishnu Kamath. "Nickel hydroxide electrodeposition from nickel nitrate solutions: mechanistic studies." Journal of Power Sources 93.1, 273-278, 2001.

[32] J. Ji, W.C. Cooper, D.B. Dreisinger, E. Peter. "Surface pH measurements during nickel electrodeposition", Journal of Applied Electrochemistry, 25, pp 642–650, 1995. 10.1007/BF00241925.

[33] J.P Hoare, "Boric acid as a catalyst in nickel plating solutions", Journal of The Electrochemical Society, Vol 134, pp 3102–3103, 1987.

[34] B.N. Popov, M.K. Yin, E.R. White, "Galvanostatic Pulse and Pulse Reverse Plating of Nickel - Iron Alloys from Electrolytes Containing Organic Compounds on a Rotating Disk Electrode", Journal of the Electrochemical Society, Vol 140, pp 1321–1330, 1993.

[35] K-M. Yin and B-T. Lin, "Effects of boric acid on the electrodeposition of iron, nickel and iron-nickel", Surface and Coatings Technology, Vol. 78, no. 1, pp 205– 210, 1996.

[36] C.E. Davalos, J.R. Lopez, H. Ruiz, A. Mendez, R. Antano-Lopez, G. Trejo, "Study of the role of boric acid during the electrochemical deposition of Ni in a sulfamate bath", International Journal of Electrochemical Science, Vol. 8, no. 7, 2013.

[37] S. Armyanov, G. Sotirova-Chakarova, "Hydrogen desorption and internal stress in nickel coatings obtained by periodic electrodeposition", Journal of The Electrochemical Society, Vol. 139, no. 12, pp 3454–3457, 1992.

[38] P.C. Andricacos, J. Locarnini, V.L. Oliver, and L.T. Romankiw. "Iron Autoanalyzer for Nickel-Iron Plating Bath", vol 3, no. 1, IBM Tech. Discl. Bull, 1988.

[39] M.C. Blakeslee, L.T. Romankiw, R.E. Acosta, S. Krongelb, B.J. Stoeber, "Electrodeposition process for fabrication of conductor in first SLM 2mm bubble memory", Journal of the Electrochemical Society, vol. 125, Issue 3, pp C152–C152, 1978.

Jeremy Murray (S'06) received the Bachelor degree (Hons.) in electronics engineering from the University of Wales, Bangor, U.K and his Ph.D. degree from the University of Edinburgh, U.K. working at the Scottish Microelectronics Centre and the school of Chemistry.

His current research interests include the fabrication of microelectromechanical systems and sensor technology. He is currently Research Programme Manager for Pyreos Limited.

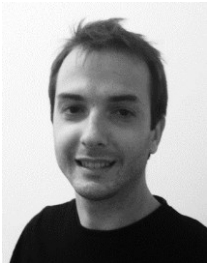

Richard Perry received an M.Chem. in Chemistry with Materials Chemistry (2011) and PhD (2016) from the University of Edinburgh, UK. During his PhD he worked looking at the fundamental aspects of electrochemical deposition and developed new baths for electrodepositing Nickel and Nickel-Iron using alternatives to boric acid. In addition, he studied the material properties for their suitability for use as a functional magnetic material in MEMS devices. He has recently completed A PGDE in Education.

Jonathan G Terry (SM '08) received his B. Eng in Electronic Engineering, M.Sc. in Microelectronic Material & Device Technology and his Ph.D. in Solid State Electronics from the University of Manchester Institute of Science and Technology (UMIST). He joined the Institute for Integrated Micro and Nano Systems (IMNS) at the University of Edinburgh in 1999 as a research fellow. He is currently a Chancellor's Fellow and Lecturer at the University of Edinburgh where his main area of interest is in the development of More-than-Moore technologies, the integration of novel fabrication processes and materials with foundry CMOS to create smart microsystems.

Stewart Smith (SM'12) received the B.Eng. (Hons.) degree in electronics and electrical engineering and the Ph.D. degree from the University of Edinburgh, Scotland, U.K., in 1997 and 2003, respectively. He is currently a Lecturer with the School of Engineering, University of Edinburgh, where he is also a member of the Research Institute for Bioengineering. His current research interests include the design and fabrication of bioelectronic and biomedical microsystems, microfluidics and biosensors, and development of test structures for MEMS and microsystems processes. He is a member of the Technical Committee for the IEEE International Conference on Microelectronic Test Structures and an Officer of the Scottish Chapter of the IEEE Electron Devices Society.

Andy Mount is a Professor and Head of Physical Chemistry at the University of Edinburgh (UoE). He is a former Royal Society of Edinburgh/SEELLD Support Research Fellow, has published over 70 papers and filed 10 patents. He has interests and expertise in electrochemical production and the combination of spectroscopic (particularly fluorescence) and electrochemical characterisation. He is Chair of the RSC Electrochemistry Group, member of the RSC Faraday Standing Committee on Conferences, founder member of the Centre for Materials Science at Edinburgh, the Edinburgh Materials Microanalysis Centre (EMMAC) and the Centre for Science under Extreme Conditions (CSEC), reviewer at Oak Ridge National Labs, and has been the Chair of Faraday Discussion 149 (2010).

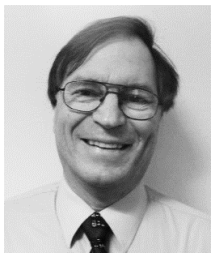

Anthony J. Walton (SM'88) is a Professor of microelectronic manufacturing with the School of Engineering, University of Edinburgh, U.K. Over the past 25 years, he has been actively involved with the semiconductor industry in a number of areas associated with silicon processing that includes both integrated circuit technology and microsystems. In particular, he has been intimately involved with the development of technologies and their integration with CMOS. He played a key role in setting up the Scottish Microelectronics Centre, which is a purpose-built facility for research and development and commercialization. He has published over 350 papers.